IEEE Access
Multidisciplinary | Rapid Review | Open Access Journal

Received April 30, 2020, accepted May 6, 2020, date of publication May 11, 2020, date of current version May 21, 2020.

Digital Object Identifier 10.1109/ACCESS.2020.2993607

Edge Information Based Image Fusion Metrics Using Fractional Order Differentiation and Sigmoidal Functions

ANIMESH SENGUPTA[1], AYAN SEAL[2,3], (Senior Member, IEEE), CHINMAYA PANIGRAHY[2], ONDREJ KREJCAR[3], AND ANIS YAZIDI[4], (Senior Member, IEEE)

[1]Vellore Institute of Technology–Chennai, Chennai 600048, India
[2]PDPM Indian Institute of Information Technology, Design and Manufacturing, Jabalpur 482005, India
[3]Center for Basic and Applied Research, Faculty of Informatics and Management, University of Hradec Kralove, 500 03 Hradec Kralove, Czech Republic
[4]Department of Computer Science, Oslo Metropolitan University, 0166 Oslo, Norway

Corresponding author: Ayan Seal (ayanseal30@ieee.org)

This work was supported in part by the project (Prediction of diseases through computer assisted diagnosis system using images captured by minimally-invasive and non-invasive modalities), Computer Science and Engineering, PDPM Indian Institute of Information Technology, Design and Manufacturing, Jabalpur, India, under Grant SPARC-MHRD-231, in part by the project of Grant Agency of Excellence, University of Hradec Kralove, Faculty of Informatics and Management, Czech Republic, under Grant UHK-FIMGE-2020, and in part by the IT4Neuro—project of the Ministry of Education, Youth and Sports of Czech Republic under Project ERDF CZ.02.1.01/0.0/0.0/18 _069/0010054.

ABSTRACT In recent years, the number of image fusion schemes presented by the research community has increased significantly. Measuring the performance of these schemes is an important issue. In this work, we introduce three quantitative fusion metrics to assess the quality of an image fusion algorithm. The proposed metrics rely on edge information that is obtained using fractional order differentiation. Edge and orientation strengths are fed into three sigmoidal functions separately for estimating the values of three normalized weighted metrics for the fused image corresponding to source images. The experiments on the multi-focus, infrared-visible and medical image fusion pairs demonstrate that the proposed fusion metrics are perceptually meaningful and outperform some of the state-of-the-art metrics.

INDEX TERMS Edge detection, fractional order differentiation, fusion metric, image fusion, sigmoidal functions.

I. INTRODUCTION

In general, the word image fusion means a method to amalgamate and coalesce all the useful complementary information acquired from multiple source images of a given scene into a single representation called fused image. Image fusion has a number of applications such as multi-focus [1]–[4], medical [5]–[9], infrared-visible [10]–[14], etc. Due to the tremendous advancement of fusion techniques, the problem of performance evaluation and assessment of image fusion techniques has gained a lot of attention within the research community [15]. The fusion methods can be evaluated in two ways, viz., qualitatively and quantitatively. The qualitative evaluation corresponds to assessing the quality of a fused image, which is carried out by human visual system (HVS). However, our naked eyes cannot continuously ascertain the quality enhanced by a fused image over the source images. Therefore, researchers are developing many quality evaluation indexes/metrics since three decades for measuring the performance of a fusion process quantitatively/objectively. Quantitative and objective evaluations are same, thus are used interchangeably in this study. Fusion metrics can be grouped into three categories, namely, statistic based, information theory based, and human perception related [16]. Root means square error (RMSE) [17], peak signal noise ratio (PSNR) [18], rate of correct classification [19], and others [20] fall in the first category. The second category consists of entropy [21], the collective cross entropy [22], mutual information (MI) [23], correlation information entropy [24], information deviation [25], and other indices [26]. Edge information (EI) [27], space resolution and spectral resolution [28], space frequency and space visibility [29], change of contrast [30], and other indexes [31] lie in the third category. Fusion metrics can also be divided into two groups based on the number of reference images. The first group consists of fusion metrics for which reference/source image is required

The associate editor coordinating the review of this manuscript and approving it for publication was Yudong Zhang.

to measure the performance. RMSE [17], signal to noise ratio [32], percentage fit error [33], mean bias [34], relative dimensionless global error [35], spectral angular mapper [36], PSNR [18], correlation coefficient [37], MI [38], structural similarity (SSIM) [39], universal quality index [36], and others [18] fall in the first group. There is no need for reference image for the second group to evaluate the performance of a fusion process. Standard deviation [21], entropy [21], cross entropy [40], spatial frequency [41], and others [18] lie in the second group.

Though there exist a number of metrics to assess fusion methods quantitatively, every metric have some drawbacks [15]. The non-reference metrics are faster to compute, however it considers only the fused image. So, the correspondence between the source images and the fused image cannot be properly judged. The reference image based metrics are widely used but are computationally expensive. The statistic based metrics are not suitable to all types of fusion applications whereas information theory based metrics are inconsistent [16]. Moreover, the human perception related metrics are subjective and hard to quantify [16]. Hence, there is no unanimously accepted fusion metric for evaluating the quality of fusion schemes. However, among the different metrics, EI [27] is frequently used to evaluate the performance of fusion methods [1], [2], [42]–[44], which efficiently quantifies the edge information of source images contained by the fused image. It uses Sobel operator to generate the edge magnitude and orientation information. However, Sobel operator is sensitive to noise and provides poor anti-noise performance [45]. Therefore, the EI metric sometimes fails to generate the desired result. In recent times, fractional order differentiation is applied to image fusion [46]–[49], which is robust to noise and improves the detection selectivity [50]. Simultaneously, fractional order differentiation better retains the detailed feature information of the image compared with the integer order differentiation like Sobel operator [49]. Motivated by the popularity of EI metric and superiority of fractional order differentiation, three novel image fusion metrics based on three sigmoidal functions, viz., tanh, arctan, and logistic are proposed in this work, which combines the robustness of the EI metric and effectiveness of the fractional order differentiation. The proposed metrics use fractional order differentiation to extract the edge information of the source images contained in the fused image. The correspondence of the proposed metrics with respect to HVS are shown using state-of-the-art fusion methods designed for multi-focus, infrared-visible, and medical image fusion. The effectiveness of the proposed metrics are demonstrated using five popular fusion metrics, namely, entropy, EI [27], MI [23], SSIM [39], and edge-dependent fusion quality index [51].

The main contributions of this paper are described as follows:

(1) Three fractional order differentiation based fusion metrics correspond to three sigmoidal functions, namely, tanh, arctan, and logistic are proposed in this work by modifying the EI metric, where fractional order differentiation is applied to quantify the edge information of the source images preserved by the fused image.
(2) The effectiveness of the proposed metrics is demonstrated using the fusion results on the multi-focus, infrared-visible, and medical image pairs obtained by popular state-of-the-art fusion methods.
(3) The competitiveness of the proposed metrics is shown using the five well known state-of-the-art fusion metrics.

The rest of this work is organized as follows. Section II presents the proposed method. In Section III, the experimental results are discussed in detail. Finally, Section IV concludes the work.

II. MATERIALS AND METHODS

A. EDGE DETECTION USING FRACTIONAL ORDER DIFFERENTIATION

Edge detection algorithm acts as an important tool in computer vision applications especially in feature detection and feature extraction. Researchers introduced integer-order differentiation operators especially order 1 [52] and order 2 [53] in gradient based and Laplacian based edge detection methods respectively. The fractional calculation is able to enhance the quality of images. Moreover, the use of an edge detection based on non-integer differentiation improves the detection selectivity of the edge information. Fractional differentiation based non-integer differentiation using Grunwald-Letnikov definition is successfully incorporated to edge detection methods [50]. The contour Robuste d'Ordre Non Entier (CRONE) detector introduced by Mathieu *et al.* is an edge detecting technique which utilizes fractional differentiation to single out edges [50]. The CRONE detector uses the cusp of derivative at inflexion point of abscissa to generate the edge detector. This technique has remarkable detection sensitivity, selectivity, and immunity to noise for order of fractional differentiation lying between $[-1, 1]$. The edges are determined by convoluting the image pixel by pixel with a predefined moving window/mask. Many masks are available in literature for edge detection. In [54], V. Garg *et al.* presented an improved Grunwald-Letnikov fractional differentiation mask. In [55], Duch *et al.* discussed two new masks by combining sobel operator and Grunwald-Letnikov fractional differential mask for 0 degree, M_0, and 90 degree, M_{90}, called Likewise-Radar Fractional order edge operators, which are shown in Eqs. (1) and (2) respectively.

$$M_0 = \begin{bmatrix} -G_2 & 0 & G_2 \\ -G_1 & 0 & G_1 \\ -G_2 & 0 & G_2 \end{bmatrix}, \tag{1}$$

$$M_{90} = \begin{bmatrix} -G_2 & -G_1 & -G_2 \\ 0 & 0 & 0 \\ G_2 & G_1 & G_2 \end{bmatrix}, \tag{2}$$

where the values of $G_i|i = 1,2$ in Eqs. (1) and (2) can be computed using Eq. (3), shown at the bottom of this page. In Eq. (3), $\Gamma(\cdot)$ is a gamma function whereas r is the order of differentiation and $r \in [0, 1]$.

In this work, these two masks, namely M_0 and M_{90} are used to convolve with the input image, I, to obtain the horizontal, I^h, and vertical, I^v, edge images.

B. EDGE SIMILARITY MEASURES

In this section, three edge similarity measures, namely, detection error rate (DER), detection common rate (DCR) and detect correct similarity (DCS) are defined [56]. These similarity measures estimate how similar an edge image is with respect to another edge image. In other words, these three measures help to calculate the similarity value between two edge images obtained by two different edge operators.

Definition 1 (Detection Error Rate): Let us consider two gray-scale edge images, namely A and B. Then the value of DER can be computed using Eq. (4).

$$DER(A, B) = \frac{|F(A \setminus B)|}{|F(B)|}, \tag{4}$$

where $F(A \setminus B)$ is the set edge pixels that appears in A but not in B whereas $F(B)$ depicts the set of edge pixels in B. The operator, $|\cdot|$, represents cardinality of a set.

Definition 2 (Detection Common Rate): The value of DCR is estimated using Eq. (5).

$$DCR(A, B) = \frac{|F(A\&B)|}{|F(B)|}, \tag{5}$$

where $F(A\&B)$ denotes the set of edge pixels appearing in both A and B.

Definition 3 (Detect Correct Similarity): The DCS is the ratio of DCR and DER, which would be computed by Eq. (6).

$$DCS(A, B) = \frac{DCR(A, B)}{DER(A, B)} = \frac{|F(A\&B)|}{|F(A \setminus B)|}. \tag{6}$$

The greater the value of DCS metric, the higher the similarity between A and B. Edge image obtained by Likewise-Radar Fractional is considered as A while B is used to represent sobel edge image for this work. The greater similarity with sobel edge detector method guarantees the fact that the chosen fractional edge detector is at par if not better than the sobel method.

Theorem 4: $DER(A, B) = DER(B, A)$ iff $A = B$ wherein A, B are images.

Proof: Since $DER(A, B)$ is directly proportional to $F(A \setminus B)$ and from the definition of Eq. (4) we can conclude that $DER(A, B)$ is directly proportional to the set difference operation of two images A and B i.e. $(A - B)$.

Now, let us consider Fig. 1 which shows two sets, namely A and B. The following two statements can be inferred from

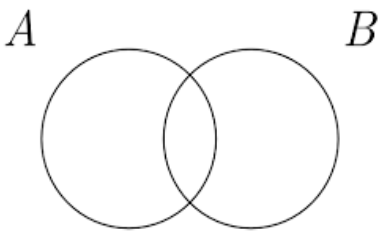

FIGURE 1. Two sets *A* and *B*.

Fig. 1 by incorporating set theory.

$$A = (A - B) \cup (A \cap B),$$
$$B = (B - A) \cup (A \cap B).$$

If $A - B = B - A$ then,

$$\begin{aligned} A &= (A - B) \cup (A \cap B) \\ &= (B - A) \cup (A \cap B) \\ &= B \end{aligned}$$

So, this proves that set difference operator is commutative i.e. $A - B = B - A$ iff $A = B$, thus same holds true for the DER operator. Thus, $DER(A, B) = DER(B, A)$ iff $A = B$ and holds false otherwise.

Theorem 5: $DCS(A, B) = DCS(B, A)$ iff, $A = B$, where A and B are images.

Proof: According to Eq. (6), DCS operator is inversely proportional to $DER(A, B)$ i.e. $F(A \setminus B)$ and directly proportional to $DCR(A, B)$ i.e. $F(A\&B)$. Also, according to the definition, $F(A \setminus B)$ is the set difference operation between image A and B i.e. $(A - B)$. Now, $F(A\&B) = F(B\&A)$ because set intersection operator is commutative in nature. But, from Theorem 4, $DER(A, B) = DER(B, A)$ iff $A = B$ and since DCS is inversely proportional to DER operator we can conclude that DCS will be commutative if and only if DER is commutative and for that to happen A should be equal to B. The converse holds false that is $DCS(A, B)$ will not be equal to $DCS(B, A)$ if A is not equal to B.

C. PROPOSED FUSION METRIC

One of the primary objectives of image fusion is to construct a fused image preserving maximum visual information from its source images to provide better visualization. In other words, fusion rules should be formulated in such a way that it can extract perceptually meaningful information from source images and transfer them into the fused image as precisely as possible so that HVS can easily identify the improvement of fused image over source images. The proposed fusion metric would extract the edge information from source and fused images using Eqs. (1) and (2) because edge information is considered as one of the perceptual visual information in computer vision applications.

$$G_i = \frac{1}{\Gamma(-r)}\left[\frac{\Gamma(i - r + 1)}{(i + 1)!}\left(\frac{r}{4} + \frac{r^2}{8}\right) + \frac{\Gamma(i - r)}{i!}\left(1 - \frac{r^2}{4}\right) + \frac{\Gamma(i - r - 1)}{(i - 1)!}\left(-\frac{r}{4} + \frac{r^2}{8}\right)\right]. \tag{3}$$

Let us consider two source images, namely A and B of size $M \times N$ pixels. Let F be the fused image of same size i.e. $M \times N$ pixels obtained by a fusion technique, which integrates A and B. The edge strengths of these three images are estimated separately using Eqs. (7), (8), and (9) [27].

$$S_A(x,y) = \sqrt{A^h(x,y)^2 + A^v(x,y)^2}, \tag{7}$$

$$S_B(x,y) = \sqrt{B^h(x,y)^2 + B^v(x,y)^2}, \tag{8}$$

$$S_F(x,y) = \sqrt{F^h(x,y)^2 + F^v(x,y)^2}, \tag{9}$$

where x and y are the x and y coordinates of the respective image. The orientations of these three images are calculated using Eqs. (10), (11), and (12) [27].

$$O_A(x,y) = tan^{-1}\left(\frac{A^h(x,y)}{A^v(x,y)}\right). \tag{10}$$

$$O_B(x,y) = tan^{-1}\left(\frac{B^h(x,y)}{B^v(x,y)}\right). \tag{11}$$

$$O_F(x,y) = tan^{-1}\left(\frac{F^h(x,y)}{F^v(x,y)}\right). \tag{12}$$

The relative edge strength and orientation of F with respect to A would be computed using Eqs. (13) and (14) respectively.

$$S_{FA}(x,y) = \begin{cases} \dfrac{S_F(x,y)}{S_A(x,y)} & \text{if } S_A(x,y) > S_F(x,y) \\ \dfrac{S_A(x,y)}{S_F(x,y)} & \text{otherwise.} \end{cases} \tag{13}$$

$$O_{FA}(x,y) = 1 - \frac{2 \times |O_A(x,y) - O_F(x,y)|}{\pi}. \tag{14}$$

Similarly, Eqs. (15) and (16) would be used to calculated edge strength and orientation of F with respect to B.

$$S_{FB}(x,y) = \begin{cases} \dfrac{S_F(x,y)}{S_B(x,y)} & \text{if } S_B(x,y) > S_F(x,y) \\ \dfrac{S_B(x,y)}{S_F(x,y)} & \text{otherwise.} \end{cases} \tag{15}$$

$$O_{FB}(x,y) = 1 - \frac{2 \times |O_B(x,y) - O_F(x,y)|}{\pi}. \tag{16}$$

The next step is to estimate edge strength and orientation retaining values using sigmoid functions. Sigmoidal functions are popularly used in neural networks as an activation function due to its bipolar transfer nature [57]. A fusion metric is binary in nature because every fusion metric provides a value within a finite range, which helps to check whether a fusion approach is either good or bad. Moreover, sigmoidal function's distinctive feature of strictly increasing and $S-$curve growth with a finite range of function value make it even more suitable for modeling a fusion metric. In [16], C.S. Xydeas *et al.* considered logistic sigmoidal function for modeling a fusion metric. The logistic function can be represented using Eq. (17).

$$\text{logistic: } f(u) = \frac{e^u}{e^u + 1}. \tag{17}$$

Hyperbolic tangent (tanh) and arcus tangent (arctan) functions are also considered as sigmoid functions, which are shown in Eqs. (18) and (19) respectively.

$$\text{tanh: } g(u) = \frac{e^u - e^{-u}}{e^u + e^{-u}}. \tag{18}$$

$$\text{arctan: } k(u) = arctan(u). \tag{19}$$

However, tanh function is the rescaled version of the logistic function and can be derived using Eq. (20).

$$g(u) = 2f(2u) - 1. \tag{20}$$

Tanh function has twice the range than that of sigmoidal function i.e. $(-1, 1)$. Since, this function is zero-centered and anti-symmetric about the origin, it leads to faster convergence. Tanh function is also widely used as a activation function and greatly excels in 2-class classification problems. Arctan function is popularly known as inverse tangent function. This function having a flatter S shape than the rest makes it a bit potent in classification problems. Thus, we can conclude that, in principal, arctan function is potentially superior to the rest functions due to the above stated reason. Sigmoidal functions are very good for modeling probabilistic type of variables, since it saturates at 0 and 1 while the tanh functions saturate at -1 and 1. Similarly, arctan saturates at $-\pi/2$ and $\pi/2$. Figure 2 shows how the three sigmoid functions vary from each other and where their saturation lies.

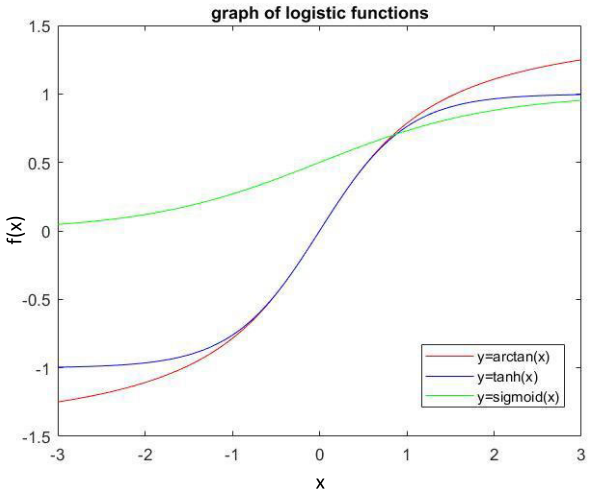

FIGURE 2. Plots of sigmoidal functions.

The perceptual loss of information in F, in terms of how good the strength and orientation values of a pixel in A that are represented in the F would be estimated using Eqs. (21) and (22), shown at the bottom of the next page, based on arctan function. Three above mentioned sigmoid functions are used in this study. However, equation of the arctan function is shown here because this is superior to other sigmoid functions. Similarly, Eqs. (23) and (24), shown at the bottom of the next page, could be used to compute the information loss of edge strength and orientation of F with respect to B.

In the above equations, the constants a, b, c, and d determine the exact shape of sigmoid functions. Edge information

at a particular pixel location (x, y), transferred from A to F can be computed using Eq. (25), shown at the bottom of this page. Similarly, Eq. (26), shown at the bottom of this page, could be used to estimate the edge information transferred from B to F.

The value of R^{FA} and R^{FB} will always lie between 0 and 1 because four constants modify arctan function and bring its range between 0 and 1 including themselves. Lesser the edge information, greater the loss of information from the source images in the fused image. Normalized weighted fusion metric, $R_Q^{\frac{F}{AB}}$, of a fusion scheme Q that operates on images A, B, and generates F is obtained using Eq. (27), shown at the bottom of this page. In Eq. (27), $W^A(x, y)$ and $W^B(x, y)$ are the weights of the edge retaining values $R^{FA}(x, y)$ and $R^{FB}(x, y)$ respectively. Here, weights would be computed by $W^A(x, y) = S_A(x, y)^L$ and $W^B(x, y) = S_B(x, y)^L$, where L is constant. In this work, $L = 1$. The value of the proposed metric, $R_Q^{\frac{F}{AB}}$, for a fused image can be calculated using Eq. (27). In order to compute edge and orientation strengths of a fused image with respect to its source images, three sigmoidal functions, namely, tanh, arctan, and logistic are used interchangeably in Eqs. (21) to (24). It means three fusion metrics are proposed based on three sigmoidal functions respectively. Since, the proposed metrics use EI metric like mechanism to investigate the quality of a fused image, higher values for the proposed metrics correspond to better fused images. In this study, the order of fractional differential edge detection method is assumed to be 1.8 because it is the best order in our experiments which is discussed in section III-E.

The values of the proposed metrics significantly depend upon the type and shape of sigmoidal functions used. Since, rescaling and reshaping of these sigmoidal functions may have profound effects over the parameter values, it is paramount to make it constant over the course of experimentation. The shape of sigmoidal functions depends on the Eqs. (28), (29), and (30).

$$logistic(x) = a(f(c(x - b)) + d). \tag{28}$$

$$arctan(x) = a(k(c(x - b)) + d). \tag{29}$$

$$tanh(x) = a(g(c(x - b)) + d). \tag{30}$$

The values of a, b, c, and d can be modified to change the shape and size of previously defined sigmoidal functions. Using these parameters, the sigmoidal functions are rescaled and reshaped. Moreover, the values of these parameters are kept constant throughout the course of experimentation. The values of these four parameters for edge and orientation strengths are set empirically, which are presented in tables 1 and 2 respectively. Figure 3 reveals the rescaled sigmoidal functions for edge and orientation strengths.

TABLE 1. Parameter values of sigmoidal functions for edge strength.

Function name	a	b	c	d
Arctan	$1/\pi$	0.5	15	0.5
Tanh	0.5	0.5	15	0.5
Logistic	0.994	0.5	15	0

TABLE 2. Parameter values of sigmoidal functions for orientation strength.

Function name	a	b	c	d
Arctan	$1/\pi$	0.8	22	0.5
Tanh	0.5	0.8	22	0.5
Logistic	0.9879	0.8	22	0

III. EXPERIMENTAL RESULTS AND DISCUSSION

A. DATABASE DESCRIPTION

The images from the SIPI image database [58] are considered to obtain the edge images using fractional order edge detection method. This database consists of frequently used images in the literature such as ''Zelda'', ''Cameraman'' etc. The first column of Fig. 4 shows some of the sample images taken from SIPI image database. In order to validate the proposed fusion quality metrics, four multi-focus images pairs (MF-1, MF-2, MF-3, and MF-4) [3], four infrared-visible image pairs (IV-1, IV-2, IV-3, and IV-4) [10], and four medical image pairs (MED-1, MED-2, MED-3, and MED-4) [2] are used in the experiments. Three color multi-focus image pairs (MF-C-1, MF-C-2, and MF-C-3) [59] are also considered to illustrate the workability of the proposed metrics. Furthermore, three gray-scale and pseudo color medical image pairs (GP-MED-1, GP-MED-2, and GP-MED-3) are used to show the effectiveness of the proposed metrics. Different image pairs are shown in the first two rows of Figs. 6, 7, 8, 9, 10, and 11 whereas Table 3 reports the size of different image pairs.

B. COMPUTATIONAL PROTOCOLS

In order to show the workability of a fusion metric, it is necessary to show the correspondence between the metric and

$$R_S^{FA}(x, y) = arctan(S_{FA}(x, y)) = a \cdot (tan^{-1}(c(S_{FA}(x, y)) - b) + d). \tag{21}$$

$$R_O^{FA}(x, y) = arctan(O_{FA}(x, y)) = a \cdot (tan^{-1}(c(O_{FA}(x, y)) - b) + d). \tag{22}$$

$$R_S^{FB}(x, y) = arctan(S_{FB}(x, y)) = a \cdot (tan^{-1}(c(S_{FB}(x, y)) - b) + d). \tag{23}$$

$$R_O^{FB}(x, y) = arctan(O_{FB}(x, y)) = a \cdot (tan^{-1}(c(O_{FB}(x, y)) - b) + d). \tag{24}$$

$$R^{FA}(x, y) = R_S^{FA}(x, y) \times R_O^{FA}(x, y). \tag{25}$$

$$R^{FB}(x, y) = R_S^{FB}(x, y) \times R_O^{FB}(x, y). \tag{26}$$

$$R_Q^{\frac{F}{AB}} = \frac{\sum_{x=1}^{M} \sum_{y=1}^{N} (R^{FA}(x, y)W^A(x, y) + R^{FB}(x, y)W^B(x, y))}{\sum_{x=1}^{M} \sum_{y=1}^{N} (W^A(x, y) + W^B(x, y))}. \tag{27}$$

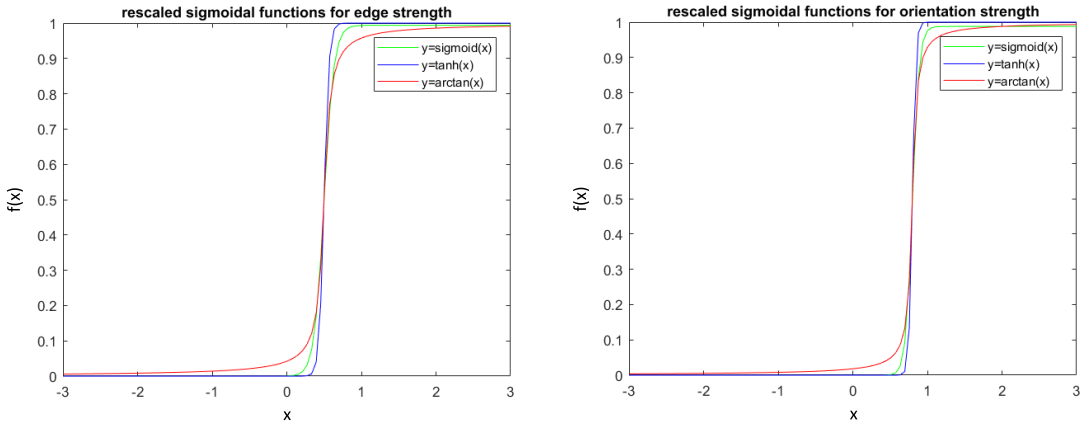

FIGURE 3. Rescaled sigmoidal functions for edge strength (left) and orientation strength (right).

TABLE 3. Size of image pairs.

Image pair	Size (In pixels)
MED-1, MED-2, MED-3, MED-4, GP-MED-1, GP-MED-2, and GP-MED-3	256×256
MF-2	384×512
IV-2	450×620
MF-3 and MF-4	480×640
IV-4	496×632
MF-1	512×512
MF-C-1, MF-C-2, and MF-C-3	520×520
IV-1	576×768
IV-3	678×917

quality of the fused image obtained by a method. Simultaneously, a good metric should be applicable to all types of fusion applications. Therefore, four types of image fusion techniques, namely, multi-focus, infrared-visible, medical, and robust are considered in this work to show the correspondence between the proposed metrics and quality of the fused images, where robust fusion methods can be applicable to all types of applications for constructing the fused image. The above fusion techniques are specially designed to work for particular image fusion applications. Different state-of-the-art image fusion methods are briefly described as follows.

Three image fusion methods, viz., quad-tree (QT) [1], non-subsampled contourlet transform with sparse representation (NSCT-SR) [2], and boundary finding based on multiscale morphological focus measure (BF-MSMFM) [3] are considered to compare the performance of the proposed metrics on the multi-focus image pairs. The QT performs the quad-tree based decomposition of the source images to obtain the fused image. In NSCT-SR, the source images are first transformed into low-pass and high-pass sub-bands using NSCT, where the low-pass sub-bands are fused using SR. On the other hand, the high-pass sub-bands are combined using max-rule. Finally, the fused image is obtained from the decomposed sub-bands. The BF-MSMFM generates the fused image by finding boundaries between the defocused and focused regions of the source images using a novel focus measure.

In order to show the effectiveness of the proposed metrics in infrared-visible image fusion, three state-of-the-art methods, namely, anisotropic diffusion and Karhunen-Loeve transform (AD-KLT) [60], two-scale using saliency detection (TS-SD) [10], and gradient transfer and total variation minimization (GT-TVM) [42]. In AD-KLT, the source images are decomposed into base and detail layers using anisotropic diffusion. The detail layers are fused using KLT whereas weighted superposition is used for the base layers. The TS-SD considers averaging filter to decompose the source images into detail and base layers, where the detail layers are fused by the weight map constructed from the visual saliency of the source images. The averaging rule is employed to obtain the fused base layer. In GT-TVM, the fusion problem is formulated as a ℓ^1-total variation minimization problem, where the data fidelity and regularization terms preserve the important intensity distribution in the infrared image and gradient variation in the visible image respectively.

The efficacy of the proposed metrics on the medical image fusion is shown using three image fusion methods, viz., Laplacian pyramid with SR (LP-SR) [2], convolutional SR (CSR) [61], and non-subsampled shearlet transform using pulse coupled neural network (NSST-PCNN) [7]. The LP-SR is similar to NSCT-SR, where LP is used instead of NSCT. In [61], Tikhonov regularization is first utilized to decompose the source images into a base and a detail layer. The fused detail layer is obtained using CSR whereas max-rule is considered to construct the fused base layer. After applying NSST to the source images, NSST-PCNN uses the parameter adaptive PCNN to fuse the high-pass sub-bands whereas fused low-pass sub-band is obtained using weighted local energy and weighted sum of eight-neighbourhood based modified Laplacian.

The robustness of the proposed metrics on the gray-scale and pseudo color medical image fusion is discussed using three recent image fusion methods, namely, information of interest in local Laplacian filtering domain (II-LLF) [62], phase congruency and local Laplacian energy in NSCT domain (PC-LLE-NSCT) [63], and Laplacian

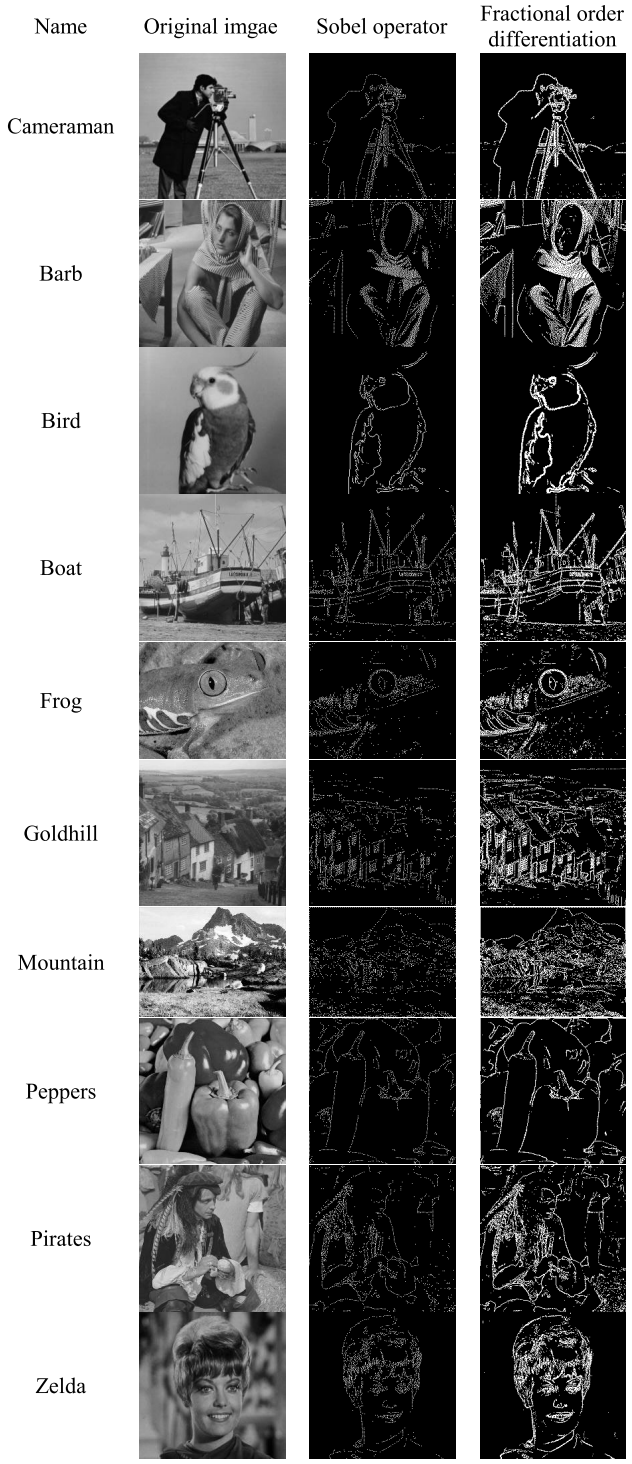

FIGURE 4. Original images, edge images obtained using sobel operator and fractional order differentiation.

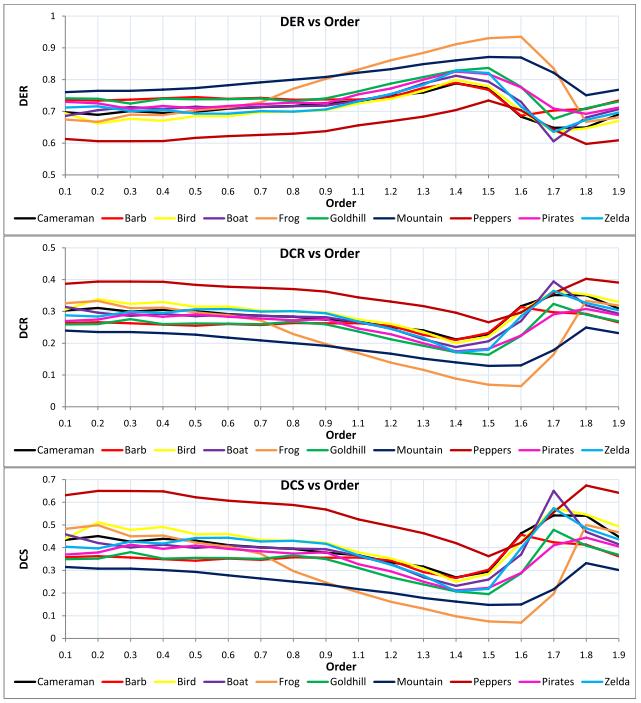

FIGURE 5. DER, DCR, and DCS values for the images shown in Fig. 4.

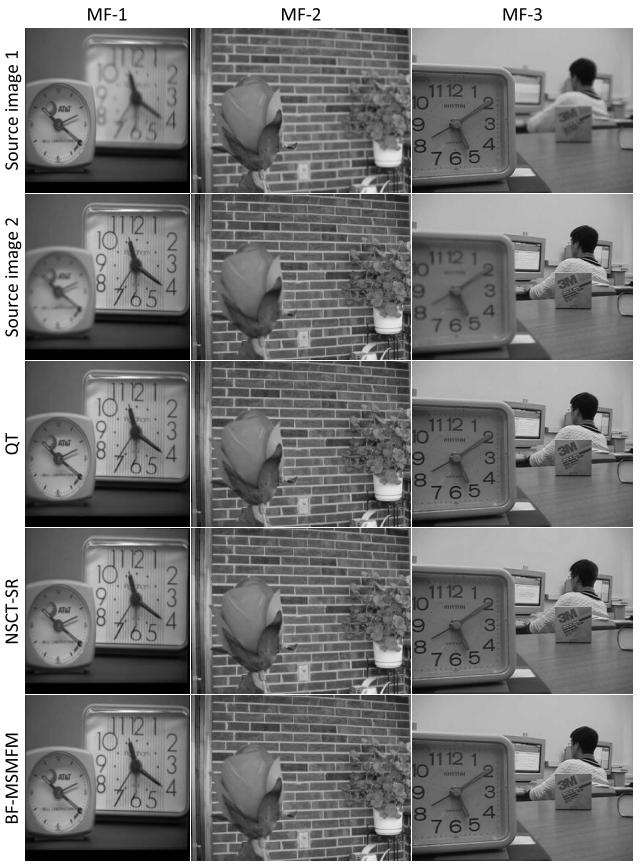

FIGURE 6. Fusion results on multi-focus image pairs.

re-decomposition (LRD) [64]. In II-LLF, LLF is first applied to source images, then the fused approximate image is obtained using a maximum local energy (MLE) rule whereas the fused residual images are generated by an information of interest based scheme and MLE rule. The fused image is reconstructed from the fused approximate and residual images. In PC-LLE-NSCT, the fused high-pass sub-bands are constructed using PC whereas LLE is used to construct the fused low-pass sub-band. The LRD first decomposes

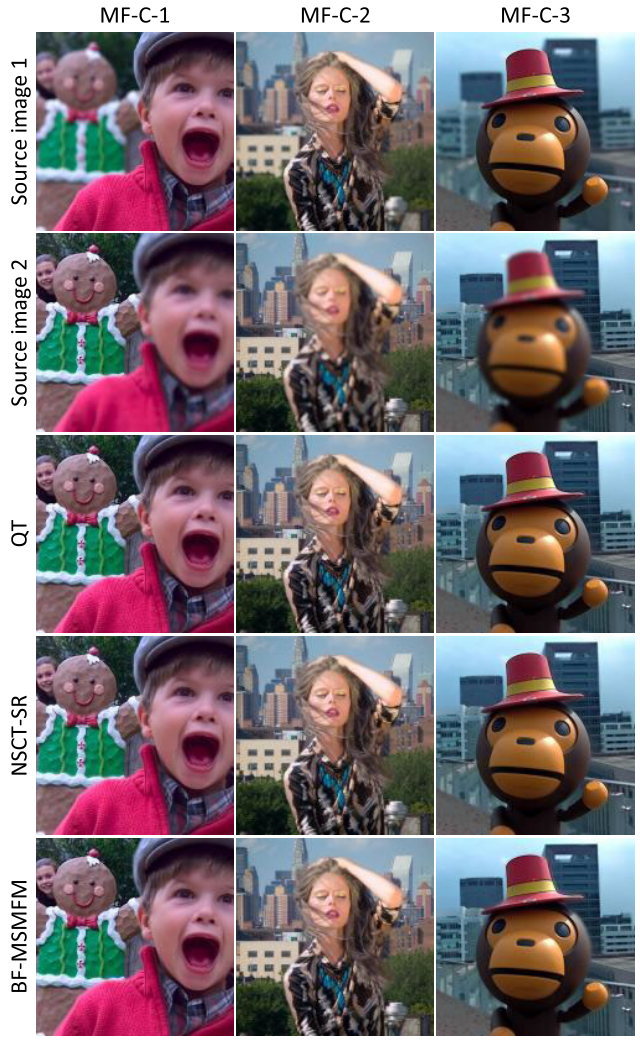

FIGURE 7. Fusion results on multi-focus color image pairs.

FIGURE 8. Fusion results on infrared-visible image pairs.

the source images into redundant, complementary, and low-pass information using Laplacian decision graph decomposition. The redundant and complementary information are fused using novel overlapping and non-overlapping domain. Low pass sub-bands are fused using MLE rule. The fused high-pass sub-bands are obtained from fused redundant and complementary information using an inverse re-decomposition scheme. Finally, fused image is constructed by applying inverse Laplacian transform.

Finally, three robust image fusion methods, namely, NSCT with spatial frequency motivated PCNN (NSCT-SF-PCNN) [43], guided filtering (GF) [44], and adaptive SR (ASR) [65] are considered to show the competitiveness of the proposed metrics with five well known state-of-the-art image fusion metrics. In NSCT-SF-PCNN, the SF of the decomposed coefficients corresponding to the source images obtained using NSCT are fed into PCNN whose outputs are utilized to get the fused image. Unlike the SR based methods that learn a single redundant dictionary, ASR learns a number of sub-dictionaries from the high quality image patches which are pre-classified using their gradient information. ASR adaptively selects a sub-dictionary to generate the fused image. In [44], the source images are first decomposed into base and detail layers using averaging filter. Then, the weight maps for these layers are obtained using GF, which are finally used to obtain the fused base and detail layers.

C. COMPUTATIONAL METRICS

The effectiveness of the proposed metrics is shown using five image fusion quality metrics, namely, entropy (E_F), EI or Petrovic's metric ($Q^{AB/F}$) [27], MI ($MI^{AB/F}$) [23], SSIM [39] and edge-dependent fusion quality index (Q_E) [51]. E_F measures the degree of information contained by the fused image, F. $Q^{AB/F}$ quantifies the edge information of the source images, A and B that is transferred to F. $MI^{AB/F}$ estimates the degree of dependency between A, B, and F. SSIM computes the similarity between the source and fused images whereas Q_E represents the edge dependent saliency information of the source images which is preserved by the fused image. Higher values of these five metrics corresponds to a better fused image.

D. PROGRAMMING ENVIRONMENT

All the experiments are performed in MATLAB R2019b on a PC with Intel(R) Core(TM) i3-5005U CPU @ 2.00GHz and 4-GB RAM. The parameters of different fusion methods are set to their default values.

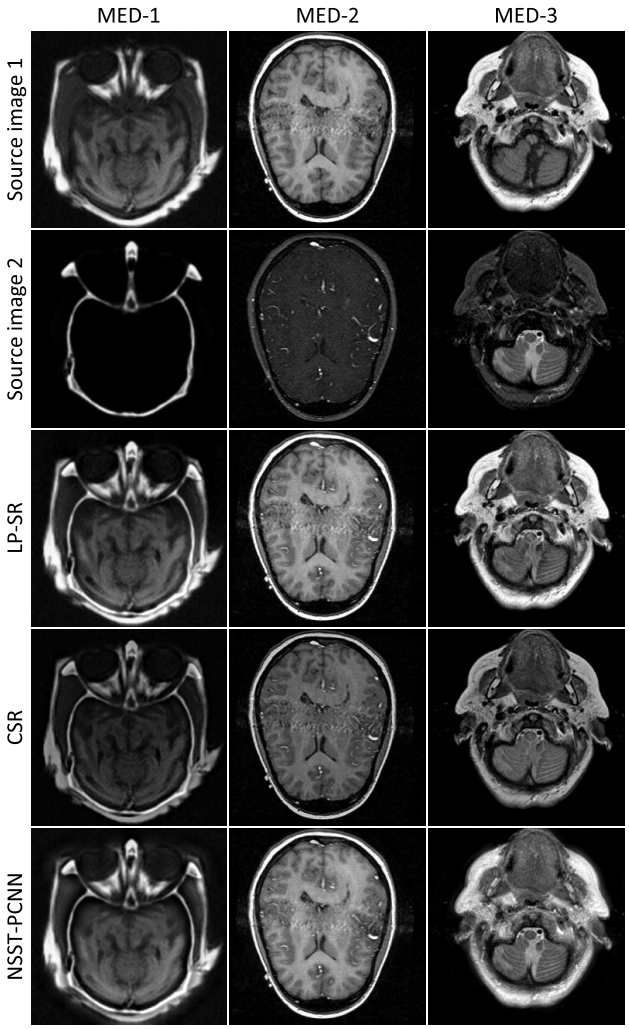

FIGURE 9. Fusion results on medical image pairs.

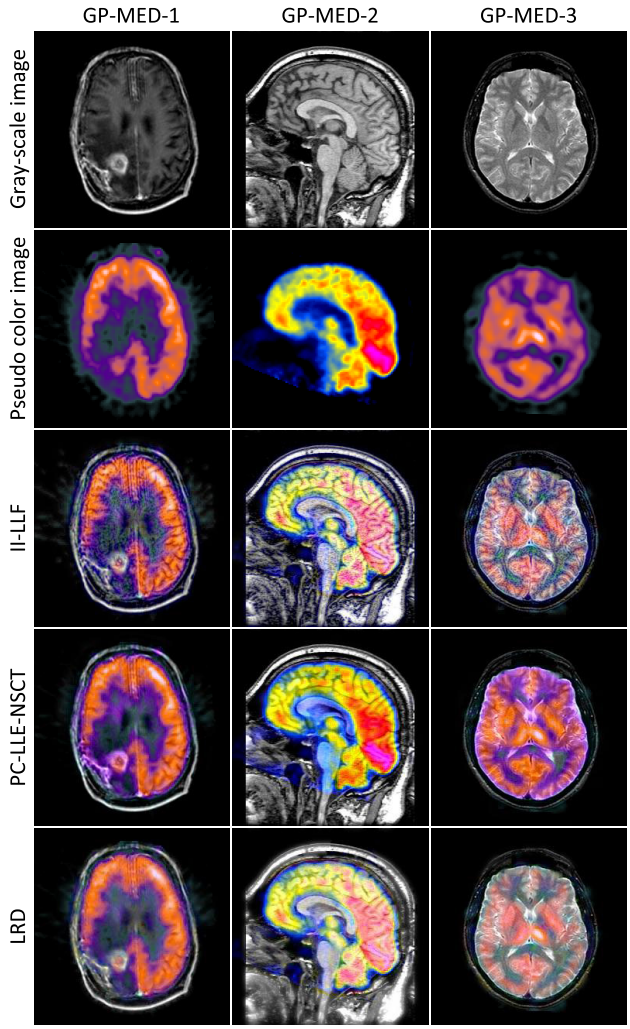

FIGURE 10. Fusion results on gray-scale and pseudo color medical image pairs.

E. DETERMINATION OF ORDER FOR EDGE DETECTION USING FRACTIONAL DIFFERENTIATION

In the first experiment, likewise-radar fractional and sobel operators are used separately to find edge images. However, the former one depends on an input parameter i.e., *order*. In order to compare the edge images obtained using likewise-radar fractional with sobel edge images, the values of *order* are varied from 0.1 with a step-size of 0.1 until getting a convergence. Here, only non integer values are considered as the values for *order* to ensure fractional order differentiation. Initially, the comparison is performed by bare eyes. Visual perception depicts that the edges obtained using fractional order method is comparable with the sobel edge detection method. But, HVS cannot always recognize the improvement achieved by an edge detection method over other methods. Hence, quantitative analysis is required. The quantitative analysis can be conducted based on the DCS values. These values are estimated for the images shown in the first column of Fig. 4.

Figure 5 shows the estimated DCS values along with DER and DCR values up to order 1.9 because the higher values of order beyond 1.9 are less convergent. In this study, we are interested in estimating edge strengths using fractional order only. Thus, the edge strengths are not calculated for the *order* 1.0 which is an integer order equivalent to the first order differentiation. Similarly, edge strengths are not considered for the zero order. It can be observed in Fig. 5 that almost all the images show an upward trend in similarity when the order is increased. The Graph of DCS vs order can be used to interpret many useful insights. The same graph depicts a very significant downfall/through in the order range of 1.3 to 1.6 while drastically increases till 1.8. The DCS values for most of the images increase in the range of 1.6 to 1.8 order level. Thus, we can infer that an order of 1.8 gives a desirable edge output, comparable to sobel operator. We can conclude from this experiment that order of 1.8 is best suitable for further processing. However, for different experiments, the best order may vary. The edge images for the images shown in the first column of Fig. 4 obtained by sobel operator and fractional order, 1.8 are shown in the second and third columns of Fig. 4 respectively. Visual perception clearly shows that the images shown in the third column of Fig. 4 provide better

TABLE 4. The values of $R_Q^{F_{AB}}$ for the fused images of multi-focus image pairs shown in Fig. 6 obtained by QT, NSCT-SR, and BF-MSMFM.

	QT			NSCT-SR			BF-MSMFM		
Image	tanh	arctan	logistic	tanh	arctan	logistic	tanh	arctan	logistic
MF-1	0.7469	**0.6683**	**0.7218**	0.7207	0.6396	0.6903	**0.7470**	0.6679	0.7216
MF-2	**0.7430**	**0.6637**	**0.7160**	0.7272	0.6448	0.6961	0.7400	0.6608	0.7128
MF-3	**0.7584**	**0.6803**	**0.7347**	0.7378	0.6563	0.7088	0.7574	0.6790	0.7333

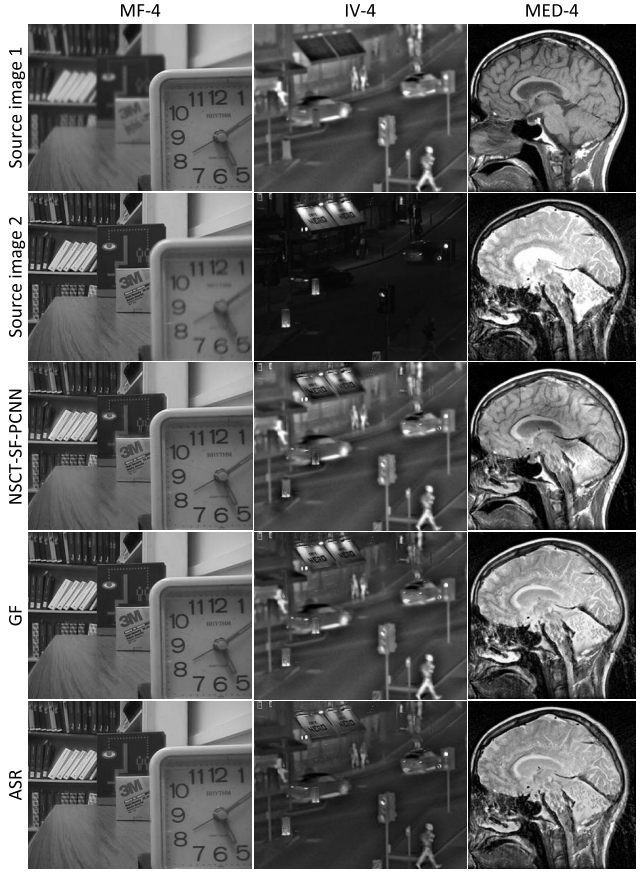

FIGURE 11. Sample image pairs and the corresponding fused images.

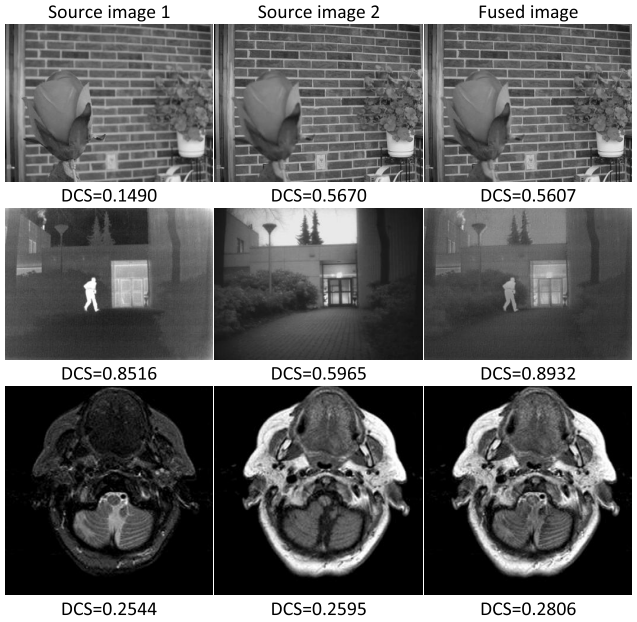

FIGURE 12. DCS values of sample image fusion pairs.

and more edges as compared to the images of second column. This proves that the fractional order differentiation is indeed detection sensitive, since it is able to detect very light edges. Moreover, an image with better visual quality is more likely to have a higher DCS value.

F. RESULTS FOR IMAGE FUSION AND PROPOSED FUSION METRICS

In the second experiment, QT, NSCT-SR, and BF-MSMFM are implemented on MF-1, MF-2, and MF-3 image pairs and the obtained fused images are shown in Fig. 6 whereas the values of $R_Q^{F_{AB}}$ for these images are reported in Table 4. It is clear from Fig. 6 that the visual quality of the fused images obtained by QT are better than NSCT-SR and BF-MSMFM except the clock boundary in the fused image of MF-1 which is better fused by BF-MSMFM. However, BF-MSMFM produces blurry left pedicel for the MF-2 image pair. Few ringing effects can be seen in the fused images generated by NSCT-SR, which are caused due to NSCT. It can be observed from Table 4 that the $R_Q^{F_{AB}}$ produces higher values for most of the fused images obtained by QT which matches with the subjective quality of the fused images. It shows the effectiveness of the proposed fusion metrics. Moreover, the values of $R_Q^{F_{AB}}$ with tanh sigmoidal function are always higher than arctan and logistic whereas arctan produces the least values of $R_Q^{F_{AB}}$.

In the next experiment, above three methods are executed on three color images pairs, viz., MF-C-1, MF-C-2, and MF-C-3. The subjective and objective results are shown in Fig. 7 and Table 5 respectively. While estimating the values of $R_Q^{F_{AB}}$ for color images, channel-wise $R_Q^{F_{AB}}$ is first calculated and then averaged to get the final $R_Q^{F_{AB}}$ value. It shows the similar trend as the second experiment suggests. The values of $R_Q^{F_{AB}}$ for the fused images of QT are always higher than NSCT-PCNN and BF-MSMFM for all the color multi-focus image pairs. Again it proves the efficiency of $R_Q^{F_{AB}}$.

In the fourth experiment, three image pairs, namely, IV-1, IV-2, and IV-3 are combined using AD-KLT, iTS-SD, and GT-TVM. The generated fused images are displayed in Fig. 8 and the corresponding $R_Q^{F_{AB}}$ values are presented in Table 6. The subjective quality of the fused images produced by TS-SD are better than AD-KLT and GT-TVM. Though GT-TVM preserves the thermal radiation in the fused images, it almost blurred the object boundaries.

TABLE 5. The values of $R_Q^{F_{AB}}$ for the fused images of color multi-focus image pairs shown in Fig. 7 obtained by QT, NSCT-SR, and BF-MSMFM.

	QT			NSCT-SR			BF-MSMFM		
Image	tanh	arctan	logistic	tanh	arctan	logistic	tanh	arctan	logistic
MF-C-1	**0.7494**	**0.6719**	**0.7256**	0.7348	0.6522	0.7047	0.7486	0.6707	0.7243
MF-C-2	**0.7234**	**0.6492**	**0.7004**	0.7096	0.6320	0.6822	0.7203	0.6457	0.6968
MF-C-3	**0.7265**	**0.6531**	**0.7044**	0.6980	0.6222	0.6707	0.7143	0.6413	0.6913

TABLE 6. The values of $R_Q^{F_{AB}}$ for the fused images of infrared-visible image pairs shown in Fig. 8 obtained by AD-KLT, TS-SD, and GT-TVM.

	AD-KLT			TS-SD			GT-TVM		
Image	tanh	arctan	logistic	tanh	arctan	logistic	tanh	arctan	logistic
IV-1	0.4972	0.4376	0.4639	**0.5119**	**0.4508**	**0.4793**	0.4584	0.4063	0.4286
IV-2	0.4728	0.4143	0.4382	**0.5363**	**0.4725**	**0.5035**	0.4049	0.3605	0.3778
IV-3	0.5007	0.4347	0.4608	**0.5504**	**0.4848**	**0.5172**	0.3294	0.3001	0.3096

TABLE 7. The values of $R_Q^{F_{AB}}$ for the fused images of medical image pairs shown in Fig. 9 obtained by LP-SR, CSR, and NSST-PCNN.

	LP-SR			CSR			NSST-PCNN		
Image	tanh	arctan	logistic	tanh	arctan	logistic	tanh	arctan	logistic
MED-1	**0.7987**	**0.7038**	**0.7627**	0.7340	0.6228	0.6756	0.7254	0.6317	0.6828
MED-2	**0.6746**	**0.6040**	**0.6489**	0.6553	0.5709	0.6178	0.5919	0.5236	0.5591
MED-3	**0.6380**	**0.5694**	**0.6111**	0.5990	0.5170	0.5558	0.4416	0.3907	0.4085

TABLE 8. The values of $R_Q^{F_{AB}}$ for the fused images of gray-scale and pseudo color medical image pairs shown in Fig. 10 obtained by II-LLF, PC-LLE-NSCT, and LRD.

	II-LLF			PC-LLE-NSCT			LRD		
Image	tanh	arctan	logistic	tanh	arctan	logistic	tanh	arctan	logistic
GP-MED-1	0.5410	0.4774	0.5095	**0.6470**	**0.5706**	**0.6139**	0.5926	0.5171	0.5536
GP-MED-2	0.7002	0.6090	0.6569	**0.7372**	**0.6516**	**0.7030**	0.6027	0.5227	0.5581
GP-MED-3	0.5611	0.4909	0.5247	**0.6595**	**0.5806**	**0.6253**	0.6394	0.5595	0.6020

TABLE 9. The values of $R_Q^{F_{AB}}$ for the fused images of image pairs shown in Fig. 11 obtained by NSCT-SF-PCNN, GF, and ASR.

Image pair	Computational protocol	E_F	$Q^{AB/F}$ [27]	$MI^{AB/F}$ [23]	$SSIM$ [39]	Q_E [51]	Proposed metrics			Rank of the fused image
							tanh	arctan	logistic	
MF-4	NSCT-SF-PCNN	7.2975	0.8866	6.2272	0.8595	0.8487	0.6627	0.5865	0.6324	3
	GF	**7.3086**	0.8925	**7.0623**	0.8616	**0.8662**	**0.7281**	**0.6501**	**0.7026**	**1**
	ASR	7.2852	**0.8951**	6.1839	**0.8721**	0.8623	0.7052	0.6229	0.6745	2
IV-4	NSCT-SF-PCNN	**6.7876**	0.8882	**3.9245**	0.6104	0.7487	0.6693	0.5913	0.6367	2
	GF	6.5308	**0.8986**	1.9196	0.6161	**0.7877**	**0.7001**	**0.6173**	**0.6674**	**1**
	ASR	6.0458	0.8672	2.1217	**0.6314**	0.6756	0.6056	0.5229	0.5610	3
MED-4	NSCT-SF-PCNN	7.3419	0.7420	3.2111	0.5754	0.4601	0.4877	0.4324	0.4575	3
	GF	**7.7459**	**0.7965**	**3.8635**	0.6139	**0.5374**	**0.6217**	**0.5459**	**0.5869**	**1**
	ASR	7.5595	0.7892	3.4978	**0.6197**	0.5280	0.5905	0.5149	0.5520	2

The quantitative evaluation as shown in Table 6 depicts the superiority of TS-SD over other two methods.

Three methods, viz., LP-SR, CSR, and NSST-PCNN are exploited on MED-1, MED-2, and MED-3 image pairs in the fifth experiment. The obtained fused images and the respective $R_Q^{F_{AB}}$ values are shown in Fig. 9 and Table 7 respectively. It is clear from Fig. 9 and Table 7 that the subjective and objective quality of the fused images obtained by LP-SR are better than CSR and NSST-PCNN. The results exhibit the effectuality of the proposed fusion metrics.

The sixth experiment is performed on GP-MED-1, GP-MED-2, and GP-MED-3 image pairs using three methods, viz., II-LLF, PC-LLE-NSCT, and LRD to show the effectiveness of the proposed metrics corresponding to gray-scale and pseudo color image fusion. The fusion results of these image pairs are shown in Fig. 10 whereas the corresponding $R_Q^{F_{AB}}$ values are reported in Table 8. It can be inferred from Fig. 10 that PC-LLE-NSCT produces well balanced fused images that mostly retain the anatomical and functional information from the gray-scale and pseudo color images respectively. Though, II-LLF transfers maximum anatomical information from the gray-scale image to the fused image, it completely fails to resemble the color components which represent the functional information. Thus, its fused images are even worst than LRD, which can be seen in the fusion results of GP-MED-3 image pair. For the GP-MED-3 image pair, II-LLF produced over exposed fused image. It is evident in Table 8 that the fused images obtained by PC-LLE-NSCT produce highest $R_Q^{F_{AB}}$ values.

In the last experiment, the performance of the proposed image fusion metrics is compared with five state-of-the-art metrics discussed in Section III-C. Here, three methods, namely, NSCT-SF-PCNN, GF, and ASR are applied on MF-4, IV-4, and MED-4 image pairs. The fused images obtained

TABLE 10. Computational time of different metrics for the fused image of MF-4 image pair obtained by NSCT-SF-PCNN.

E_F	$Q^{AB/F}$	$MI^{AB/F}$	$SSIM$	Q_E	Proposed metrics		
					tanh	arctan	logistic
0.0169	5.9508	0.0458	0.2014	0.3023	2.4629	2.0488	2.3626

by these methods are shown in Fig. 11 and the values of different metrics for these fused images are stated in Table 9. The last column of Table 9 represents the rank of the fused images based on HVS. It can be seen in Fig. 11 that GF outperforms other two methods. Ideally, the subjective and objective qualities of a fused image should follow the same trend. It is clear from this experiment that the proposed fusion metrics along with Q_E obey this order. Thus, the proposed fusion metrics can be used to evaluate the performance of a fusion technique.

It is clear from the above stated experiments that for most of the cases, the proposed metrics produce higher values for the better fused images. Therefore, the method which produces better fused images is prone to generate higher values for the proposed metrics. Here, a better fused image corresponds to a fused image with better visual quality. In other words, the proposed metrics are directly proportional to the qualitative evaluation of a fused image. Thus, it can be said that the proposed metrics resembles the HVS. The values of the proposed metrics lie between 0 and 1 which occurs due to the rescaling of three corresponding sigmoidal functions. Moreover, the values of the proposed metric for tanh sigmoidal function varies from 0.3294 to 0.7987 with a dynamic range 0.4693. The dynamic ranges of arctan and logistic sigmoidal functions are 0.4037 and 0.4531 respectively. Simultaneously, tanh provides higher values of $R_Q^{\frac{F}{AB}}$ because it approaches its asymptotes more faster than logistic and arctan sigmoidal functions. Furthermore, the performance of the proposed metrics is comparable with the state-of-the-art metrics.

Remarks: Fusion techniques are desired to produce a fused image which preserves the complementary salient edge features of the source images. In other words, the fused image has more quantitative edge information than the source images. Thus, source images are prone to have less DCS values. Figure 12 shows the DCS values of three image fusion image pairs and corresponding sample fused images. The fused images have quite higher or almost same DCS values. Therefore, in this work, fractional differentiation based edge information metric is proposed to measure the visual saliency preserved in the fused image.

G. COMPUTATIONAL COST

In order to compare the running time of different metrics, the MF-4 image pair is selected. Table 10 reports the running time of different metrics required to assess the fused image of MF-4 image pair obtained by NSCT-SF-PCNN. It can be seen in Table 10 that E_F and $Q^{AB/F}$ are computationally most and least efficient respectively. The proposed metric based on tanh and arctan sigmoidal function take highest and lowest time among the proposed metrics. Moreover, Table 11 depicts the average running time of different methods used in this study. The running time of the proposed metrics may be reduced to some extent by using efficient programming languages like Python and C++.

TABLE 11. Average computational time of different methods.

Type of image pair		Method	Time
Multi-focus	Gray-scale	QT	0.6999
		NSCT-SR	75.3833
		BF-MSMFM	2.2546
	Color	QT	3.4142
		NSCT-SR	156.7132
		BF-MSMFM	5.8841
Infrared-visible		AD-KLT	3.9056
		TS-SD	0.1028
		GT-TVM	25.4188
Medical		LP-SR	0.0779
		CSR	95.4288
		NSST-PCNN	36.7167
Gray-pseudocolor Medical		II-LLF	438.8341
		LLE-NSCT	16.4157
		LRD	341.6461
Miscellaneous		NSCT-SF-PCNN	426.1078
		GF	1.4497
		ASR	615.3184

IV. CONCLUSION

Edge information using fractional order differentiation based fusion metrics based on three sigmoidal functions, namely, tanh, arctan, and logistic functions are proposed in this study to assess the quality of image fusion schemes quantitatively. The proposed metrics rely on the type of sigmoidal functions. The characteristics are almost same for the three sigmoidal functions. Moreover, the shape and size of the curves obtained using these functions are controlled by four parameters. So, these parameters are tuned in such a way that the range of the proposed metrics lie between 0 and 1. These three functions take edge and orientation strengths as inputs and estimates normalized weighted fusion metric, which helps to judge the quality of a fusion algorithm with the help of fused image and the corresponding source images. Here, source images are called reference images as well. The tanh sigmoidal function provides higher values for the proposed metric with the best dynamic range. The typical range of the normalized weighted fusion metric is from 0 to 1. A lower value i.e. close to 0 corresponds to a poor fusion algorithm whereas higher values i.e. close to 1 depict better fusion algorithms. The experiments on multi-focus, infrared-visible, and medical image pairs using fifteen fusion algorithms show that the proposed metrics are effective in representing the response of HVS. The competitiveness of the proposed metrics are shown using five popular state-of-the-art fusion metrics. Future work lies in devising some fusion rules using fractional order differentiation to accomplish image fusion. The computational cost of the proposed metrics can be reduced using C++, Python, and parallel programming.

REFERENCES

[1] X. Bai, Y. Zhang, F. Zhou, and B. Xue, "Quadtree-based multi-focus image fusion using a weighted focus-measure," *Inf. Fusion*, vol. 22, pp. 105–118, Mar. 2015.

[2] Y. Liu, S. Liu, and Z. Wang, "A general framework for image fusion based on multi-scale transform and sparse representation," *Inf. Fusion*, vol. 24, pp. 147–164, Jul. 2015.

[3] Y. Zhang, X. Bai, and T. Wang, "Boundary finding based multi-focus image fusion through multi-scale morphological focus-measure," *Inf. Fusion*, vol. 35, pp. 81–101, May 2017.

[4] C. Panigrahy, A. Seal, and N. K. Mahato, "Fractal dimension based parameter adaptive dual channel PCNN for multi-focus image fusion," *Opt. Lasers Eng.*, vol. 133, Oct. 2020, Art. no. 106141.

[5] Z. Zhu, Y. Chai, H. Yin, Y. Li, and Z. Liu, "A novel dictionary learning approach for multi-modality medical image fusion," *Neurocomputing*, vol. 214, pp. 471–482, Nov. 2016.

[6] A. Seal, D. Bhattacharjee, M. Nasipuri, D. Rodríguez-Esparragón, E. Menasalvas, and C. Gonzalo-Martin, "PET-CT image fusion using random forest and à-trous wavelet transform," *Int. J. Numer. Methods Biomed. Eng.*, vol. 34, no. 3, p. e2933, Oct. 2017.

[7] M. Yin, X. Liu, Y. Liu, and X. Chen, "Medical image fusion with parameter-adaptive pulse coupled neural network in nonsubsampled shearlet transform domain," *IEEE Trans. Instrum. Meas.*, vol. 68, no. 1, pp. 49–64, Jan. 2019.

[8] Z. Zhu, H. Yin, Y. Chai, Y. Li, and G. Qi, "A novel multi-modality image fusion method based on image decomposition and sparse representation," *Inf. Sci.*, vol. 432, pp. 516–529, Mar. 2018.

[9] C. Panigrahy, A. Seal, and N. Mahato, "MRI and SPECT image fusion using a weighted parameter adaptive dual channel PCNN," *IEEE Signal Process. Lett.*, early access, Apr. 20, 2000, doi: 10.1109/LSP.2020.2989054.

[10] D. P. Bavirisetti and R. Dhuli, "Two-scale image fusion of visible and infrared images using saliency detection," *Infr. Phys. Technol.*, vol. 76, pp. 52–64, May 2016.

[11] A. Seal and C. Panigrahy, "Human authentication based on fusion of thermal and visible face images," *Multimedia Tools Appl.*, vol. 78, no. 21, pp. 30373–30395, Nov. 2019.

[12] A. Seal, D. Bhattacharjee, M. Nasipuri, C. Gonzalo-Martin, and E. Menasalvas, "Fusion of visible and thermal images using a directed search method for face recognition," *Int. J. Pattern Recognit. Artif. Intell.*, vol. 31, no. 4, Apr. 2017, Art. no. 1756005.

[13] A. Seal, D. Bhattacharjee, and M. Nasipuri, "Human face recognition using random forest based fusion of à-trous wavelet transform coefficients from thermal and visible images," *AEU-Int. J. Electron. Commun.*, vol. 70, no. 8, pp. 1041–1049, Aug. 2016.

[14] A. Seal, D. Bhattacharjee, M. Nasipuri, C. Gonzalo-Martin, and E. Menasalvas, "À-trous wavelet transform-based hybrid image fusion for face recognition using region classifiers," *Expert Syst.*, vol. 35, no. 6, p. e12307, Jul. 2018.

[15] B. Li, R. Li, Z. Liu, C. Li, and Z. Wang, "An objective non-reference metric based on arimoto entropy for assessing the quality of fused images," *Entropy*, vol. 21, no. 9, p. 879, Sep. 2019.

[16] L. Yan, Y. Liu, B. Xiao, Y. Xia, and M. Fu, "A quantitative performance evaluation index for image fusion: Normalized perception mutual information," in *Proc. 31st Chin. Control Conf.*, Hefei, China, 2012, pp. 3783–3788.

[17] R. Hong, W. Cao, J. Pang, and J. Jiang, "Directional projection based image fusion quality metric," *Inf. Sci.*, vol. 281, pp. 611–619, Oct. 2014.

[18] P. Jagalingam and A. V. Hegde, "A review of quality metrics for fused image," *Aquatic Procedia*, vol. 4, pp. 133–142, Jan. 2015.

[19] Z. Zhang and R. S. Blum, "A categorization of multiscale-decomposition-based image fusion schemes with a performance study for a digital camera application," *Proc. IEEE*, vol. 87, no. 8, pp. 1315–1326, Aug. 1999.

[20] D. Windridge and J. Kittler, "Performance measures of the tomographic classifier fusion methodology," *Int. J. Pattern Recognit. Artif. Intell.*, vol. 19, no. 6, pp. 731–753, Sep. 2005.

[21] W. Wang and F. Chang, "A multi-focus image fusion method based on Laplacian pyramid," *J. Comput.*, vol. 6, no. 12, pp. 2559–2566, 2011.

[22] C. Ramesh and T. Ranjith, "Fusion performance measures and a lifting wavelet transform based algorithm for image fusion," in *Proc. 5th Int. Conf. Inf. Fusion*, Annapolis, MD, USA, 2002, pp. 317–320.

[23] G. Qu, D. Zhang, and P. Yan, "Information measure for performance of image fusion," *Electron. Lett.*, vol. 38, no. 7, pp. 313–315, Mar. 2002.

[24] Q. Wang, Y. Shen, Y. Zhang, and J. Q. Zhang, "A quantitative method for evaluating the performances of hyperspectral image fusion," *IEEE Trans. Instrum. Meas.*, vol. 52, no. 4, pp. 1041–1047, Aug. 2003.

[25] Q. Wang, Y. Shen, Y. Zhang, and J. Q. Zhang, "Fast quantitative correlation analysis and information deviation analysis for evaluating the performances of image fusion techniques," *IEEE Trans. Instrum. Meas.*, vol. 53, no. 5, pp. 1441–1447, Oct. 2004.

[26] A. Ilie, R. Raskar, and J. Yu, "Gradient domain context enhancement for fixed cameras," *Int. J. Pattern Recognit. Artif. Intell.*, vol. 19, no. 4, pp. 533–549, Jun. 2005.

[27] C. S. Xydeas and V. Petrović, "Objective image fusion performance measure," *Electron. Lett.*, vol. 36, no. 4, pp. 308–309, Feb. 2000.

[28] V. S. Petrovic and C. S. Xydeas, "Gradient-based multiresolution image fusion," *IEEE Trans. Image Process.*, vol. 13, no. 2, pp. 228–237, Feb. 2004.

[29] J. F. Reinoso, "Cartographic evaluation of image fusion methods when no precise registration is possible," *Imag. Sci. J.*, vol. 57, no. 5, pp. 280–292, Oct. 2009.

[30] H. Chen and P. K. Varshney, "A human perception inspired quality metric for image fusion based on regional information," *Inf. Fusion*, vol. 8, no. 2, pp. 193–207, Apr. 2007.

[31] Z. Wang, D. Ziou, C. Armenakis, D. Li, and Q. Li, "A comparative analysis of image fusion methods," *IEEE Trans. Geosci. Remote Sens.*, vol. 43, no. 6, pp. 1391–1402, Jun. 2005.

[32] Yuhendra, I. Alimuddin, J. T. S. Sumantyo, and H. Kuze, "Assessment of pan-sharpening methods applied to image fusion of remotely sensed multi-band data," *Int. J. Appl. Earth Observ. Geoinf.*, vol. 18, pp. 165–175, Aug. 2012.

[33] V. P. S. Naidu, "Discrete cosine transform-based image fusion," *Defence Sci. J.*, vol. 60, no. 1, pp. 48–54, Jan. 2010.

[34] Y. Yusuf, J. T. S. Sumantyo, and H. Kuze, "Spectral information analysis of image fusion data for remote sensing applications," *Geocarto Int.*, vol. 28, no. 4, pp. 291–310, Jul. 2013.

[35] Q. Du, N. H. Younan, R. King, and V. P. Shah, "On the performance evaluation of pan-sharpening techniques," *IEEE Geosci. Remote Sens. Lett.*, vol. 4, no. 4, pp. 518–522, Oct. 2007.

[36] L. Alparone, B. Aiazzi, S. Baronti, A. Garzelli, F. Nencini, and M. Selva, "Multispectral and panchromatic data fusion assessment without reference," *Photogramm. Eng. Remote Sens.*, vol. 74, no. 2, pp. 193–200, Feb. 2008.

[37] X. X. Zhu and R. Bamler, "A sparse image fusion algorithm with application to pan-sharpening," *IEEE Trans. Geosci. Remote Sens.*, vol. 51, no. 5, pp. 2827–2836, May 2013.

[38] J. P. W. Pluim, J. B. A. Maintz, and M. A. Viergever, "Mutual-information-based registration of medical images: A survey," *IEEE Trans. Med. Imag.*, vol. 22, no. 8, pp. 986–1004, Aug. 2003.

[39] Z. Wang, A. C. Bovik, H. R. Sheikh, and E. P. Simoncelli, "Image quality assessment: From error visibility to structural similarity," *IEEE Trans. Image Process.*, vol. 13, no. 4, pp. 600–612, Apr. 2004.

[40] M. B. A. Haghighat, A. Aghagolzadeh, and H. Seyedarabi, "A non-reference image fusion metric based on mutual information of image features," *Comput. Electr. Eng.*, vol. 37, no. 5, pp. 744–756, Sep. 2011.

[41] B. Yang, Z.-L. Jing, and H.-T. Zhao, "Review of pixel-level image fusion," *J. Shanghai Jiaotong Univ. Sci.*, vol. 15, no. 1, pp. 6–12, Feb. 2010.

[42] J. Ma, C. Chen, C. Li, and J. Huang, "Infrared and visible image fusion via gradient transfer and total variation minimization," *Inf. Fusion*, vol. 31, pp. 100–109, Sep. 2016.

[43] X.-B. Qu, J.-W. Yan, H.-Z. Xiao, and Z.-Q. Zhu, "Image fusion algorithm based on spatial frequency-motivated pulse coupled neural networks in nonsubsampled contourlet transform domain," *Acta Automat. Sinica*, vol. 34, no. 12, pp. 1508–1514, Dec. 2008.

[44] S. Li, X. Kang, and J. Hu, "Image fusion with guided filtering," *IEEE Trans. Image Process.*, vol. 22, no. 7, pp. 2864–2875, Jul. 2013.

[45] W. Gao, X. Zhang, L. Yang, and H. Liu, "An improved sobel edge detection," in *Proc. 3rd Int. Conf. Comput. Sci. Inf. Technol.*, Chengdu, China, Jul. 2010, pp. 67–71.

[46] J.-J. Mei, Y. Dong, and T.-Z. Huang, "Simultaneous image fusion and denoising by using fractional-order gradient information," *J. Comput. Appl. Math.*, vol. 351, pp. 212–227, May 2019.

[47] H. Li, Z. Yu, and C. Mao, "Fractional differential and variational method for image fusion and super-resolution," *Neurocomputing*, vol. 171, pp. 138–148, Jan. 2016.

[48] A. Azarang and H. Ghassemian, "Application of fractional-order differentiation in multispectral image fusion," *Remote Sens. Lett.*, vol. 9, no. 1, pp. 91–100, Jan. 2018.

[49] J. Li, G. Yuan, and H. Fan, "Multispectral image fusion using fractional-order differential and guided filtering," *IEEE Photon. J.*, vol. 11, no. 6, pp. 91–100, Dec. 2019.
[50] B. Mathieu, P. Melchior, A. Oustaloup, and C. Ceyral, "Fractional differentiation for edge detection," *Signal Process.*, vol. 83, no. 11, pp. 2421–2432, Nov. 2003.
[51] G. Piella and H. Heijmans, "A new quality metric for image fusion," in *Proc. Int. Conf. Image Process.*, Barcelona, Spain, Sep. 2003, p. III-173.
[52] J. Canny, "A computational approach to edge detection," *IEEE Trans. Pattern Anal. Mach. Intell.*, vol. PAMI-8, no. 6, pp. 679–698, Nov. 1986.
[53] A. Oustaloup, B. Mathieu, and P. Melchior, "Edge detection using non integer derivation," in *Proc. 10th ECCTD*, Copenhagen, Denmark, 1991, pp. 3–6.
[54] V. Garg and K. Singh, "An improved Grunwald-Letnikov fractional differential mask for image texture enhancement," *Int. J. Adv. Comput. Sci. Appl.*, vol. 3, no. 3, pp. 130–135, Mar. 2012.
[55] P. Duch, S. Blaszczyk, M. Laski, R. Krzeszewski, and P. Ostalczyk, "Likewise–radar fractional-order edge detector," *IFAC Proc. Volumes*, vol. 46, no. 1, pp. 647–652, Feb. 2013.
[56] C. B. Gao, J. L. Zhou, J. R. Hu, and F. N. Lang, "Edge detection of colour image based on quaternion fractional differential," *IET Image Process.*, vol. 5, no. 3, pp. 261–272, Apr. 2011.
[57] P. D. B. Harrington, "Sigmoid transfer functions in backpropagation neural networks," *Anal. Chem.*, vol. 65, no. 15, pp. 2167–2168, Aug. 1993.
[58] *SIPI IMage Database—Misc*. Accessed: Aug. 13, 2018. [Online]. Available: http://sipi.usc.edu/database/database.php?volume=misc
[59] M. Nejati, S. Samavi, and S. Shirani, "Multi-focus image fusion using dictionary-based sparse representation," *Inf. Fusion*, vol. 25, pp. 72–84, Sep. 2015.
[60] D. P. Bavirisetti and R. Dhuli, "Fusion of infrared and visible sensor images based on anisotropic diffusion and karhunen-loeve transform," *IEEE Sensors J.*, vol. 16, no. 1, pp. 203–209, Jan. 2016.
[61] Y. Liu, X. Chen, R. K. Ward, and Z. Jane Wang, "Image fusion with convolutional sparse representation," *IEEE Signal Process. Lett.*, vol. 23, no. 12, pp. 1882–1886, Dec. 2016.
[62] J. Du, W. Li, and B. Xiao, "Anatomical-functional image fusion by information of interest in local Laplacian filtering domain," *IEEE Trans. Image Process.*, vol. 26, no. 12, pp. 5855–5866, Dec. 2017.
[63] Z. Zhu, M. Zheng, G. Qi, D. Wang, and Y. Xiang, "A phase congruency and local Laplacian energy based multi-modality medical image fusion method in NSCT domain," *IEEE Access*, vol. 7, pp. 20811–20824, 2019.
[64] X. Li, X. Guo, P. Han, X. Wang, H. Li, and T. Luo, "Laplacian re-decomposition for multimodal medical image fusion," *IEEE Trans. Instrum. Meas.*, early access, Feb. 20, 2020, doi: 10.1109/TIM.2020.2975405.
[65] Y. Liu and Z. Wang, "Simultaneous image fusion and denoising with adaptive sparse representation," *IET Image Process.*, vol. 9, no. 5, pp. 347–357, May 2015.

ANIMESH SENGUPTA received the B.Tech. degree in engineering from the Vellore Institute of Technology–Chennai, Chennai, India. His current research interests include image processing and pattern recognition.

AYAN SEAL (Senior Member, IEEE) received the Ph.D. degree in engineering from Jadavpur University, Kolkata, India, in 2014. He visited the Universidad Politecnica de Madrid, Spain, as a Visiting Research Scholar. He is currently an Assistant Professor with the Computer Science and Engineering Department, PDPM Indian Institute of Information Technology, Design and Manufacturing, Jabalpur, India. He has authored or coauthored of several journals, conferences and book chapters in the area of biometric and medical image processing. His current research interests include image processing and pattern recognition. He was a recipient of several awards. Recently, he received Sir Visvesvaraya Young Faculty Research Fellowship from Media Lab Asia, Ministry of Electronics and Information Technology, Government of India.

CHINMAYA PANIGRAHY received the B.Tech. degrees in computer science and engineering from B.P.U.T, Rourkela, India, in 2011, and the M.Tech. degree from V.S.S.U.T., Burla, India, in 2015. He visited the Universidad Politecnica de Madrid, Spain, as a Visiting Research Scholar. He is currently an Institute Ph.D. Research Scholar with the Computer Science and Engineering Department, PDPM Indian Institute of Information Technology, Design and Manufacturing, Jabalpur, India. His current research interests include fractal study, image processing, and pattern recognition.

ONDREJ KREJCAR received the Ph.D. degree in technical cybernetics from the Technical University of Ostrava, Czech Republic, in 2008.

He is currently a Full Professor of systems engineering and informatics with the University of Hradec Kralove, Czech Republic. He is also the Vice Dean for science and research of the Faculty of Informatics and Management, UHK. At present, he is also the Director of the Center for Basic and Applied Research, the University of Hradec Kralove. At the University of Hradec Kralove, he is a guarantee of the doctoral study program in Applied Informatics, where he is focusing on lecturing on Smart Approaches to the Development of Information Systems and Applications in Ubiquitous Computing Environments. His H-index is 18, with more than 1000 citations received in the Web of science. His research interests include control systems, smart sensors, ubiquitous computing, manufacturing, wireless technology, portable devices, biomedicine, image segmentation and recognition, biometrics, technical cybernetics, and ubiquitous computing. His second area of interest is in Biomedicine (image analysis), as well as Biotelemetric System Architecture (portable device architecture, wireless biosensors), development of applications for mobile devices with use of remote or embedded biomedical sensors. In 2018, he was the 14th top peer reviewer in Multidisciplinary in the World according to Publons and a Top Reviewer in the Global Peer Review Awards 2019 by Publons. He has been a Vice-Leader and a Management Committee member at WG4 at project COST CA17136, since 2018. He has also been a Management Committee member substitute at project COST CA16226, since 2017. Since 2014 until 2019, he has also been the Deputy Chairman of the Panel 7 (Processing Industry, Robotics, and Electrical Engineering) of the Epsilon Program, Technological Agency of the Czech Republic. Since 2019, he has also been the Chairman of the Program Committee of the KAPPA Program, and the Technological Agency of the Czech Republic as a Regulator of the EEA/Norwegian Financial Mechanism in the Czech Republic. Since 2020, he has also been the Chairman of the Panel 1 (Computer, Physical and Chemical Sciences) of the ZETA Program, Technological Agency of the Czech Republic. He is on the editorial board of the MDPI *Sensors* journal JCR index, and several other ESCI indexed journals.

ANIS YAZIDI (Senior Member, IEEE) received the M.Sc. and Ph.D. degrees from the University of Agder, Grimstad, Norway, in 2008 and 2012, respectively. He was a Researcher with Teknova AS, Grimstad. He is currently a Full Professor with the Department of Computer Science, Oslo Metropolitan University, Oslo, Norway, where he is leading the Research Group in applied artificial intelligence. His current research interests include machine learning, learning automata, stochastic optimization, and autonomous computing.